Seismic evidence for a melt-depleted lower crust on Mars: transcrustal differentiation on a stagnant-lid planet

T. Mackay-Champion*[1,2], M. Anderson Loake[3], R. Palin[1], J. Wade[1], and J.-M. Kendall[1]

[1]Department of Earth Sciences, University of Oxford, South Parks Road, Oxford, UK
[2]School of Earth Sciences, University of Bristol, Bristol, UK.
[3]Department of Statistics, University of Oxford, South Parks Road, Oxford, UK

October 20, 2025

The crust of Mars preserves a record of early planetary evolution in the absence of plate tectonics, offering a unique perspective on the development of terrestrial planets. Seismic data from NASA's InSight mission reveal a stratified crust with an intracrustal seismic discontinuity at ~24 km, overlying an interpreted crust–mantle boundary at ~38 km. Using phase equilibrium modelling integrated with petrophysics and Bayesian statistics, we show that this intracrustal discontinuity marks a transition from mafic to ultramafic lithologies and interpret the lowermost ultramafic layer as a ~14 km-thick, melt-depleted cumulate zone overlying the petrologic crust–mantle boundary. Thermal modelling indicates that such a melt-depleted layer could not have formed under ambient temperature conditions; instead, it requires an elevated heat flow likely driven by mantle upwelling and magmatic intrusion, promoting magmatic differentiation and partial melting within the crust. Together with prior evidence for evolved melts and upper-crustal differentiation, our results indicate that Mars once hosted vertically-integrated transcrustal magmatic systems akin to those common on Earth. This provides evidence that significant geochemical differentiation does not require plate tectonic activity and should be prevalent in all hot rocky bodies of sufficient size.

One of the fundamental questions in planetary science is whether planets without plate tectonics can develop a complex, differentiated, tertiary crust. As a stagnant-lid planet, Mars provides the clearest opportunity to test this idea. Its crustal evolution occupies an intermediate position between Earth's extensively reworked crust and the largely primordial surfaces of the Moon and Mercury[1], making it a key reference point for understanding planetary differentiation and thermal evolution. At the same time, the absence of tectonic recycling has allowed much of Mars's original crustal architecture to remain

*Corresponding author: tmackaychampion@gmail.com

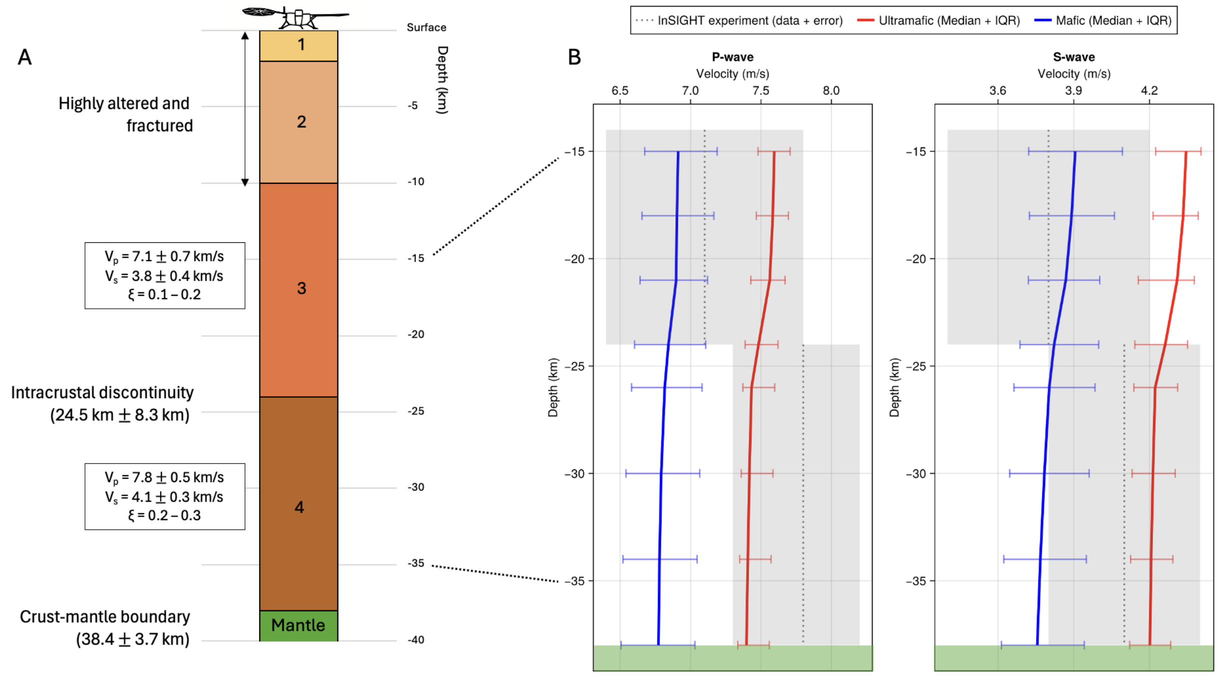

Figure 1: (A) Structure of the Martian subsurface beneath InSight. Schematic four-layer model with depth ranges and seismic velocity[3] and anisotropy constraints[6]. (B) Seismic profiles and forward-model comparisons. Observed P- and S-wave velocity profiles from InSight (grey dashed line: mean velocity; grey shaded region: ±1 standard deviation), compared to forward-modelled envelopes for ultramafic (red) and mafic (blue) compositions under assumed areotherms. Layer 3 matches mafic models; Layer 4 is inconsistent with mafic P-wave velocities in particular, but consistent with ultramafic compositions.

preserved, offering a rare geological record of early planetary processes. Understanding the structure of the Martian crust is therefore central to constraining how terrestrial planets evolve—including their chemical differentiation, lithospheric rheology, and potential for hydrosphere development[45].

Recent seismic observations from NASA's InSight mission have provided new constraints on the Martian interior, revealing a distinctly stratified crust (Fig. 1A). The upper 1.2–2 km comprises cemented, water-saturated basaltic sediment underlain by ~8 km of highly fractured basaltic or felsic rock[3;4]. These layers have experienced extensive impact-induced fracturing and likely host significant quantities of water-ice and hydrated minerals[4]. Numerous studies then identify an intracrustal discontinuity at a depth of 20–24 km[3;5;6], which coincides with a marked increase in radial anisotropy[6]. Interpretations for this layer have ranged from an ancient fossil moho[7] to basaltic layering in the lower crust[6]. Beneath this interface lies the crust-mantle boundary at ~38 km[6;8;9]. The uncertainty surrounding the composition and petrological significance of the 20–24 km interface represents a major outstanding question in the structure and evolution of the Martian crust and is the focus of this study.

Bayesian Petrophysical Modelling

To constrain the lithological character of the subsurface layers above (Layer 3) and below (Layer 4) this intracrustal interface, we integrate phase equilibrium modelling with mineral physics calculations. This provides a thermodynamic framework connecting bulk composition and state variables (pressure and temperature) to phase relations and seismic properties. A curated database of calculated and measured Martian mafic ($45 < \mathrm{SiO_2}\ \mathrm{wt\%} < 52$) and ultramafic ($\mathrm{SiO_2}\ \mathrm{wt\%} < 52$) compositions was used to forward-model seismic velocities under early- and present-day Martian areotherms for a range of potential bulk-rock compositions representative of each layer. The early areotherm defined the equilibrium mineral assemblage, whereas the present-day areotherm was used to calculate seismic velocities assuming the same assemblage remained metastable under current thermal conditions. The calculated seismic velocities are compared directly with the seismic velocity models of Drilleau et al.[3], derived from InSight data (Fig. 1B). This model places the intracrustal interface at a depth of 24.5 ± 8.3 km. The mean value of 24.5 km is adopted in our analysis, consistent with previous constraints[5]. This seismic velocity model was obtained from the joint inversion of receiver functions and surface-wave dispersion data using a fully probabilistic Markov Chain Monte Carlo framework. This provides formal uncertainty bounds on the derived velocities, while using the prior constraints on crustal structure provided by previous studies[8–12]. The resulting models are also consistent with independent datasets[10;11]. While this geophysical inversion is primarily sensitive to S-wave velocity, we include the model P-wave velocities in our analysis and apply equal weighting to both observations.

The median and interquartile ranges of the seismic velocities for the modelled mafic and ultramafic datasets define distinct depth-dependent envelopes (Fig. 1B). The mafic sample set reproduces seismic velocities consistent with the uncertainty range of Layer 3. In contrast, Layer 4 is inadequately represented by mafic compositions, especially in P-wave velocities, but aligns with the seismic characteristics expected for ultramafic lithologies. This distinction is quantitatively supported by Bayesian classification, performed using a range of prior probabilities and evaluated with a Gaussian likelihood function incorporating the report velocity uncertainty[3]. Under uniform priors, Layer 3 has a 85.8 % probability of being mafic, while Layer 4 has a 90.5 % probability of being ultramafic. The ultramafic classification of Layer 4 remains stable across a range of prior probabilities, which is consistent with the distribution of log-likelihoods for each layer (Supplementary Fig. S1). The classification also remains robust when evaluated using a broader likelihood function that imposes a smaller penalty on outlying compositions (Supplementary Table 1).

Table 1: Posterior probability estimates for Layer 3 and Layer 4. Prior probability is the probability assigned to a parameter before considering the data; posterior probability is the probability of the parameter after incorporating the data. M = mafic, UM = ultramafic. Under uniform priors, Layer 4 is 90.5 % likely to be of ultramafic composition, while Layer 3 is 85.8 % likely to be of mafic composition.

Prior(M)	Prior(UM)	Posterior(M)	Posterior(UM)
0.5	0.5	0.858031276	0.141968724
0.6	0.4	0.900652785	0.099347215
0.7	0.3	0.933784532	0.066215468
0.8	0.2	0.9602784	0.0397216
0.9	0.1	0.981947583	0.018052417
1.0	0.0	1.000000000	0.000000000

Layer 3

Prior(M)	Prior(UM)	Posterior(M)	Posterior(UM)
0.5	0.5	0.094870579	0.905129421
0.6	0.4	0.135861251	0.864138749
0.7	0.3	0.196507628	0.803492372
0.8	0.2	0.295406235	0.704593765
0.9	0.1	0.485419205	0.514580795
1.0	0.0	1.000000000	0.000000000

Layer 4

Consequently, our results indicate that the intracrustal, Layer-3/Layer-4 interface at 24.5 ± 8.3 km represents the transition from a mafic to ultramafic composition. A Latin Hypercube Sampling uncertainty analysis confirms that this conclusion is robust across a wide range of plausible areotherms, redox states, water contents, and sample subsets (Supplementary Table S2). However, the crust–mantle boundary on Mars is located at a depth of ~38 km[3;5;9]. Together, these observations indicate the presence of a thick ultramafic zone at the base of the Martian crust. We interpret this as a sequence of melt-depleted, ultramafic cumulates in the Martian lower crust, consistent with radial seismic anisotropy indicating lithological layering between 20–35 km[6] and with terrestrial analogues[13]. The seismic Moho marks the top of this sequence at 24 km, whereas the petrologic Moho at 38 km represents the true crust–mantle boundary.

Melting conditions along an ambient Martian areotherm

The presence of melt-depleted ultramafic cumulates at the base of the Martian crust may be explained by either: (1) fractionation of a mafic magma intruded into the base of the Martian crust, likely sourced from upwelling mantle; (2) partial melting of a formerly mafic lower crust. Both processes are known to have occurred during the Archean eon on Earth, playing a key role in the formation of the early continental crust[14;15]. Partial melting of the lower crust requires the Martian areotherm to exceed the

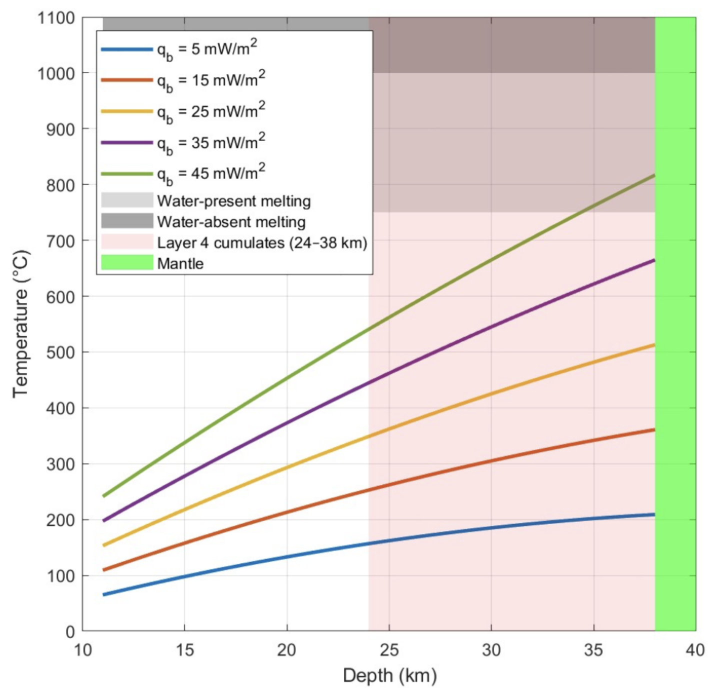

Figure 2: Areotherms on Mars for a 38 km-thick crust. Areotherms consider both basalt heat flux and radiogenic heating. Note that only a 45 mW m^{-2} (~22 °C km^{-1}) heat flux is capable of inducing partial melting within the crust and only under water-saturated conditions. Anhydrous melting at a depth of 24 km is only achieved with a heat flux of 90 mW m^{-2} (~40 °C km^{-1}).

solidus of the lower crustal lithologies. Assuming a broadly basaltic composition, this corresponds to ~750 °C and ~1000 °C for the water-saturated and anhydrous solidus respectively. Previous studies suggest that ambient crustal heat flow on Mars most likely ranged between 5–45 mW m^{-2} (~6–22 °C/km for a 38 km thick crust) during the Noachian[16;45]. Under these thermal conditions, partial melting of the lower crust at the InSight landing site would be impossible, as the Martian areotherm does not intersect the water-saturated solidus within the relevant depth range of 24–38 km (Fig. 2). These findings are consistent with previous work, which concluded that the crust beneath the northern lowlands did not exceed its melting temperature at any stage in Mars' geological evolution during or after the Noachian[45]. Partial melting of the Martian lower crust to form ultramafic cumulates would have required an anomalously high heat flow, on the order of 90 mW m^{-2} (~40 °C/km), to reach the anhydrous solidus at a depth of 24 km.

A transcrustal magma system

Given these thermal constraints, the formation of these cumulates within the Martian lower crust must have involved either: (1) unusually high local heat flow sufficient to induce in situ partial melting, or (2) the intrusion and subsequent fractionation of substantial volumes of mantle-derived mafic magma. In practice, however, distinguishing between partial melting and fractionation is somewhat artificial, as the two processes may be inherently coupled. Partial melting requires an external heat source, most effectively provided by mantle upwelling, and mantle upwelling produces mantle-derived magmas through decompression melting. Thus, enhanced heat flow and magmatic intrusion may be viewed as complementary aspects of a single magmatic event[17;18]. The emplacement of these magmas would have elevated the local areotherm sufficiently to trigger partial melting of the surrounding crust, while the intruding melts themselves underwent progressive magmatic differentiation[18]. The inferred mantle upwelling that initiated these processes may account for the recently identified sub-crustal interface at 52 ± 9 km beneath InSight[7], a feature comparable to structures observed above terrestrial mantle plumes[19].

This dynamic coupling between intrusion, heat transfer, and crustal melting mirrors analogous processes on Earth, which generate deep crustal hot zones (DCHZs)[17]. In such environments, repeated injections of mantle-derived basaltic magma supply both the material for magmatic differentiation and the thermal energy required to elevate the geotherm and drive partial melting of the surrounding crust. The seismic velocities observed for the lower crust are fully consistent with an elevated temperature of formation (Supplementary Fig. S5). Rapid melt–crystal segregation in such zones produces refractory ultramafic cumulates while allowing evolved residual melts to rise buoyantly to shallower crustal levels[13]. These processes are capable of producing substantial accumulations of ultramafic cumulates; for example, seismic data from the Aleutian arc indicate the presence of a ~10 km-thick layer of ultramafic cumulates beneath the seismic Moho[20]. Heat released during magma intrusion also promotes partial melting of adjacent mafic crust and subsequent assimilation of these melts into the residual magma, resulting in magmas with mixed crust and mantle signatures[21]. The ascending residual melts likely undergo further differentiation during cooling and crystallization within upper crustal reservoirs. Collectively, these vertically integrated processes—lower crustal melt intrusion, accumulation, fractionation, and partial melting coupled with upper crustal magma storage and evolution—define a transcrustal magmatic system (Fig. 3) comprising a mush-dominated, melt-depleted, lower crust that feeds transient, low-crystallinity magma chambers in the upper crust[13].

Our results reveal the presence of such a melt-depleted, ultramafic lower crust beneath the InSight landing site, while multiple independent datasets—seismic, orbital, and petrological—collectively support the presence of upper- to mid-crustal magma reservoirs. Seismic observations, for example, point to felsic lithologies within the upper 10 km[4], consistent with crystallized, evolved melts that would be produced and expelled from a melt-depleted lower crust. The evolved melts produced during formation of the melt-depleted lower crust must have ascended buoyantly through the predominantly mafic primary crust of Mars; some melts likely stalled in transient mid- to upper-crustal reservoirs to form crustal components analogous to Earth's Archean tonalite–trondhjemite–granodiorite (TTG) suites[22], while others may have reached the surface[23]. On Earth, the formation of TTG magmas marked a critical step in stabilizing the earliest continental nuclei, providing a buoyant, refractory lithosphere that resisted recycling and served as the foundation for later continental growth. The presence of such evolved melt compositions on Mars is supported by orbital spectroscopic observations that reveal feldspar-rich, silica-enhanced lithologies in Terra Cimmeria[23].

Further petrological evidence supports the presence of vertically integrated geochemical differentiation within the Martian crust: Firstly, the northern lowlands of Mars is known to have hosted volcanism

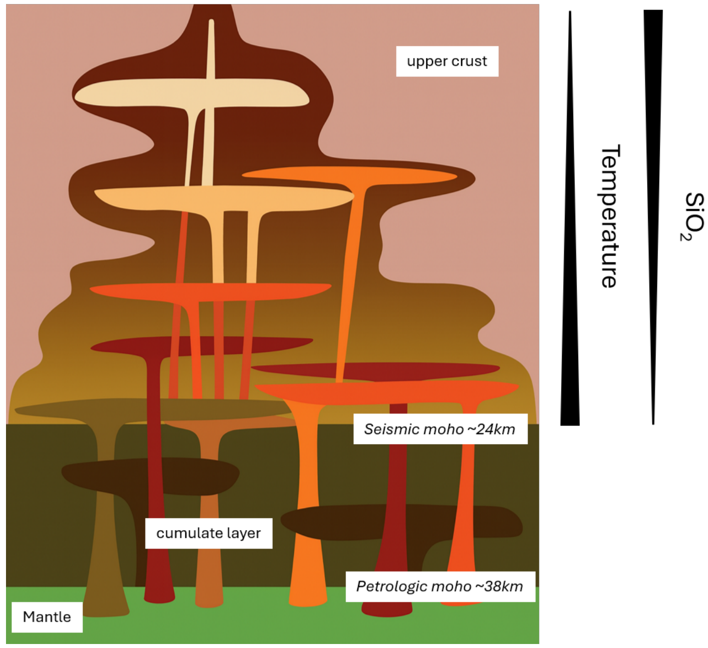

Figure 3: A transcrustal magmatic system on Mars, modified after an Earth analogue[13]. Colours indicate degrees of magmatic differentiation, with lighter tones corresponding to more evolved melts, and the gradient reflects decreasing temperature upward. The seismic Moho lies above the petrologic Moho.

throughout much of its history necessitating upper crustal magmatic systems[24]. Secondly, olivine cumulates found in Jezero crater, on the boundary of the northern lowlands and southern highlands, are interpreted to have formed through shallow intrusion into the Martian crust or emplacement within older lava flows[25]. Finally, the nakhlite and chassignite Martian meteorites record multi-level petrogenesis spanning the lower to upper crust[26], consistent with the assimilation–fractional crystallization processes required to generate evolved Martian crustal materials[27]. While geographically disparate, these observations likely represent magmatic processes that also occurred within the upper crust of the InSight region. Indeed, the widespread detection of a 20–24 km seismic discontinuity across the northern hemisphere[5;6] suggests that lower crustal melt depletion on Mars is a widespread phenomenon. This observation also tentatively strengthens the hypothesis that mantle upwelling beneath the northern hemisphere may have played a key role in generating the Martian northern–southern hemispheric dichotomy[28]. The recognition of a transcrustal magmatic system on Mars implies that large-scale crustal differentiation is a fundamental process in rocky planets, not contingent on plate tectonics. Such processes should be prevalent in all hot rocky bodies of sufficient size.

References

1. Taylor, S. R. & McLennan, S. M. *Planetary Crusts: Their Composition, Origin and Evolution* (Cambridge University Press, 2009).

2. Lee, C.-T. *et al.* Crustal thickness effects on chemical differentiation and hydrology on Mars. *Earth and Planetary Science Letters* **651**, 119155 (2025). URL https://linkinghub.elsevier.com/retrieve/pii/S0012821X24005879.

3. Drilleau, M. *et al.* Structure of the Martian Crust Below InSight From Surface Waves and Body Waves Generated by Nearby Meteoroid Impacts. *Geophysical Research Letters* **50**, e2023GL104601 (2023). URL https://agupubs.onlinelibrary.wiley.com/doi/10.1029/2023GL104601.

4. Knapmeyer-Endrun, B. *et al.* Porosity and hydrous alteration of the Martian crust from InSight seismic data. *Physics of the Earth and Planetary Interiors* **366**, 107383 (2025). URL https://linkinghub.elsevier.com/retrieve/pii/S0031920125000779.

5. Lognonné, P. *et al.* Mars Seismology. *Annual Review of Earth and Planetary Sciences* **51**, 643–670 (2023). URL https://www.annualreviews.org/content/journals/10.1146/annurev-earth-031621-073318.

6. Beghein, C. & Li, J. Seismic anisotropy layering in the Martian lowlands crust. *Physics of the Earth and Planetary Interiors* **368**, 107453 (2025). URL https://linkinghub.elsevier.com/retrieve/pii/S0031920125001475.

7. Sun, W. *et al.* Geophysical evidence of progressive Noachian crustal thickening on Mars revealed by meteorite impacts. *Earth and Planetary Science Letters* **669**, 119598 (2025). URL https://linkinghub.elsevier.com/retrieve/pii/S0012821X25003966.

8. Knapmeyer-Endrun, B. *et al.* Thickness and structure of the martian crust from InSight seismic data. *Science* **373**, 438–443 (2021). URL https://www.science.org/doi/10.1126/science.abf8966.

9. Kim, D. *et al.* Improving Constraints on Planetary Interiors With PPs Receiver Functions. *Journal of Geophysical Research: Planets* **126**, e2021JE006983 (2021). URL https://agupubs.onlinelibrary.wiley.com/doi/10.1029/2021JE006983.

10. Joshi, R. *et al.* Joint Inversion of Receiver Functions and Apparent Incidence Angles to Determine the Crustal Structure of Mars. *Geophysical Research Letters* **50**, e2022GL100469 (2023). URL https://agupubs.onlinelibrary.wiley.com/doi/10.1029/2022GL100469.

11. Shi, J. *et al.* High-Frequency Receiver Functions With Event S1222a Reveal a Discontinuity in the Martian Shallow Crust. *Geophysical Research Letters* **50**, e2022GL101627 (2023). URL https://agupubs.onlinelibrary.wiley.com/doi/10.1029/2022GL101627.

12. Carrasco, S. *et al.* Constraints for the Martian Crustal Structure From Rayleigh Waves Ellipticity of Large Seismic Events. *Geophysical Research Letters* **50**, e2023GL104816 (2023). URL https://agupubs.onlinelibrary.wiley.com/doi/10.1029/2023GL104816.

13. Sparks, R. S. J. *et al.* Formation and dynamics of magma reservoirs. *Philosophical Transactions of the Royal Society A: Mathematical, Physical and Engineering Sciences* **377**, 20180019 (2019). URL https://royalsocietypublishing.org/doi/10.1098/rsta.2018.0019.

14. Zhang, L. & Szilas, K. Eoarchean ultramafic rocks represent crustal cumulates: A case study of the Narssaq ultramafic body, southern West Greenland. *Earth and Planetary Science Letters* **625**, 118508 (2024). URL https://linkinghub.elsevier.com/retrieve/pii/S0012821X23005204.

15. Palin, R. M., White, R. W. & Green, E. C. Partial melting of metabasic rocks and the generation of tonalitic–trondhjemitic–granodioritic (TTG) crust in the Archaean: Constraints from phase equilibrium modelling. *Precambrian Research* **287**, 73–90 (2016). URL https://linkinghub.elsevier.com/retrieve/pii/S0301926816302431.

16. Ojha, L., Buffo, J., Karunatillake, S. & Siegler, M. Groundwater production from geothermal heating on early Mars and implication for early martian habitability. *Science Advances* **6**, eabb1669 (2020). URL https://www.science.org/doi/10.1126/sciadv.abb1669.

17. Annen, C., Blundy, J. D. & Sparks, R. S. J. The Genesis of Intermediate and Silicic Magmas in Deep Crustal Hot Zones. *Journal of Petrology* **47**, 505–539 (2006). URL http://academic.oup.com/petrology/article/47/3/505/1536924/The-Genesis-of-Intermediate-and-Silicic-Magmas-in.

18. Jackson, M. D., Blundy, J. & Sparks, R. S. J. Chemical differentiation, cold storage and remobilization of magma in the Earth's crust. *Nature* **564**, 405–409 (2018). URL https://www.nature.com/articles/s41586-018-0746-2.

19. Ayele, A., Stuart, G. & Kendall, J.-M. Insights into rifting from shear wave splitting and receiver functions: an example from Ethiopia. *Geophysical Journal International* **157**, 354–362 (2004). URL https://academic.oup.com/gji/article-lookup/doi/10.1111/j.1365-246X.2004.02206.x.

20. Fliedner, M. M. & Klemperer, S. L. Crustal structure transition from oceanic arc to continental arc, eastern Aleutian Islands and Alaska Peninsula. *Earth and Planetary Science Letters* **179**, 567–579 (2000). URL https://linkinghub.elsevier.com/retrieve/pii/S0012821X00001424.

21. Solano, J. M. S., Jackson, M. D., Sparks, R. S. J., Blundy, J. D. & Annen, C. Melt Segregation in Deep Crustal Hot Zones: a Mechanism for Chemical Differentiation, Crustal Assimilation and the Formation of Evolved Magmas. *Journal of Petrology* **53**, 1999–2026 (2012). URL https://academic.oup.com/petrology/article-lookup/doi/10.1093/petrology/egs041.

22. Moyen, J.-F. & Martin, H. Forty years of TTG research. *Lithos* **148**, 312–336 (2012). URL https://linkinghub.elsevier.com/retrieve/pii/S0024493712002332.

23. Payré, V., Salvatore, M. R. & Edwards, C. S. An Evolved Early Crust Exposed on Mars Revealed Through Spectroscopy. *Geophysical Research Letters* **49**, e2022GL099639 (2022). URL https://agupubs.onlinelibrary.wiley.com/doi/10.1029/2022GL099639.

24. Head, J. W., Kreslavsky, M. A. & Pratt, S. Northern lowlands of Mars: Evidence for widespread volcanic flooding and tectonic deformation in the Hesperian Period. *Journal of Geophysical Research: Planets* **107** (2002). URL https://agupubs.onlinelibrary.wiley.com/doi/10.1029/2000JE001445.

25. Liu, Y. *et al.* An olivine cumulate outcrop on the floor of Jezero crater, Mars. *Science* **377**, 1513–1519 (2022). URL https://www.science.org/doi/10.1126/science.abo2756.

26. Ostwald, A., Udry, A., Gross, J., Day, J. M. & Griffin, S. Complex zoning in the nakhlite and chassignite martian meteorites reveals multi-stage petrogenesis and undercooling during crystallization. *Geochimica et Cosmochimica Acta* **380**, 1–17 (2024). URL https://linkinghub.elsevier.com/retrieve/pii/S0016703724003302.

27. Ostwald, A., Udry, A., Payré, V., Gazel, E. & Wu, P. The role of assimilation and fractional crystallization in the evolution of the Mars crust. *Earth and Planetary Science Letters* **585**, 117514 (2022). URL https://linkinghub.elsevier.com/retrieve/pii/S0012821X22001509.

28. Zhong, S. & Zuber, M. T. Degree-1 mantle convection and the crustal dichotomy on Mars. *Earth and Planetary Science Letters* **189**, 75–84 (2001). URL https://linkinghub.elsevier.com/retrieve/pii/S0012821X01003454.

29. Connolly, J. Computation of Phase Equilibria by Linear Programming: A Tool for Geodynamic Modeling and Its Application to Subduction Zone Decarbonation. *Earth and Planetary Science Letters* **236**, 524–541 (2005).

Methods

Geochemical database and sample selection

The geochemical database includes 883 samples compiled from calculated and measured Martian rocks[30–38]. The database covers a wide range of compositions (Supplementary Fig. S2). For this study, mafic samples were defined as those containing $45–52$ wt% SiO_2, corresponding to a basaltic composition. The resulting subset is shown in Supplementary Fig. S3. Ultramafic samples were defined by SiO_2 contents below 45 wt%. To minimize the influence of surface alteration, the ultramafic subset was further refined by excluding samples with $FeO_t > 30$ wt%, $Na_2O > 1$ wt%, $K_2O > 0.25$ wt%, or $MgO < 10$ wt%. The final ultramafic subset is presented in Supplementary Fig. S4.

Phase equilibrium modelling and forward seismic modelling

Stable phase assemblages and elastic properties were computed with the MAGEMin software[39]. The behaviour of mafic samples was modelled using x-eos optimized for metabasite compositions[40], with $X\mathrm{Fe}^{3+} = 0.1$ and $H_2O\ wt\% = 0$. An extended ultramafic x-eos database[40;41], provided as standard within the MAGEMin software, was used for modelling the ultramafic samples. The same $X\mathrm{Fe}^{3+}$ and $H_2O\ wt\%$ assumptions were used.

We modelled the physical properties of mineral assemblages stable at 15–38 km along areotherms of 16 °C/km (representing metamorphism on early Mars) and 10 °C/km (representing metastable assemblages on present-day Mars). The early Mars value corresponds to the median of estimated geotherms ranging from 12–20 °C/km[42]. For present-day Mars, the 10 °C km^{-1} gradient was taken from Hoffman (2001), which is consistent with recent heat-flux estimates for the Martian surface[43]. Although the upper boundary of Layer 3 is at approximately 10–11 km, the modelling was performed from 15 to 38 km to ensure that the temperature of metamorphism was at least 200 °C, making the conditions suitable for phase equilibrium modelling.

Seismic velocities for the equilibrium phase assemblage were computed as follows[44]:

$$v_P = \sqrt{\frac{K_b + \frac{4}{3}K_s}{\rho}} \tag{1}$$

$$v_S = \sqrt{\frac{K_s}{\rho}} \tag{2}$$

Where v_P is the P-wave velocity, v_S is the S-wave velocity, ρ is the density, K_b is the adiabatic bulk modulus, and K_s is the elastic shear modulus.

The adiabatic bulk modulus is calculated from the thermodynamic data as:

$$K_b = -\frac{\delta G_{\mathrm{sys}}}{\delta P^2}\left[\frac{\delta^2 G_{\mathrm{sys}}}{\delta P^2} + \left(\frac{\delta}{\delta P}\frac{\delta G_{\mathrm{sys}}}{\delta T}\right)^2 \frac{1}{\frac{\delta^2 G_{\mathrm{sys}}}{\delta T^2}}\right]^{-1} \tag{3}$$

Shear moduli cannot be computed from thermodynamic data and are therefore calculated using an empirical relation[44]:

$$K_S = K_S^0 + T\frac{\delta K_S}{\delta T} + P\frac{\delta K_S}{\delta P} \tag{4}$$

The shear moduli of the relevant phases used in this study are taken from the database provided in $PerpleX$[29]. Bulk seismic velocities are calculated using Voigt–Reuss–Hill averaging of the velocities of the constituent phases, weighted by their volume fractions[44]. Because sensitivity kernels were not available in the original geophysical inversion, the seismic velocities for Layer 3 were estimated as the arithmetic mean of the predicted velocities at depths of 15, 18, 21, and 24 km. Similarly, the velocities for Layer 4 were calculated as the arithmetic mean of the predictions at 26, 30, 34, and 38 km. This approach assumes that the inversion is equally sensitive to seismic properties at all depths within each layer.

Bayesian classification

We computed likelihoods of the observed InSight velocities given the modelled distributions for mafic and ultramafic classes and combined them with priors to obtain posterior probabilities for each layer. Priors were varied from uniform (0.5/0.5) to strongly skewed against ultramafic to assess robustness (Table S1). Log-likelihood distributions for each class and layer are shown in Supplementary Fig. S1. Layer 4 exhibits substantially higher likelihood under the ultramafic model than under the mafic model, whereas Layer 3 shows the converse. The method is further documented below: We employ a Bayesian model selection framework to evaluate two competing compositional hypotheses—mafic versus ultramafic—and determine which provides the better explanation of the InSight seismic data. Each model generates predictions based on a range of possible compositions, which define the model's parameter space $\theta \in \Theta$. The compositions for each model were taken from a compilation of literature data. For each candidate composition, the model predicts seismic velocities $\boldsymbol{\mu} = [\mu_1, \ldots, \mu_n]$, which are compared to the observed measurements $\mathbf{y} = [y_1, \ldots, y_n]$, assuming Gaussian observational uncertainties $\boldsymbol{\sigma} = [\sigma_1, \ldots, \sigma_n]$. The log-likelihood under Gaussian error assumptions is:

$$\log \mathcal{L}(\mathbf{y} \mid \boldsymbol{\mu}, \boldsymbol{\sigma}) = -\frac{1}{2}\sum_{i=1}^{n}\left[\log(2\pi\sigma_i^2) + \frac{(y_i - \mu_i)^2}{\sigma_i^2}\right] \tag{5}$$

To account for uncertainty in the true composition, we integrate the likelihood over all candidate compositions $\theta \in \Theta$, weighted by their prior probabilities. This gives the marginal likelihood for model M, also called the model evidence, quantifying how well the model explains the data across the space of compositions:

$$p(\mathbf{y} \mid M) = \int_\Theta p(\mathbf{y} \mid \theta, M)\, p(\theta \mid M)\, d\theta \tag{6}$$

Since the integral is intractable, we approximate it using the finite set of sampled compositions $\{\theta_k\}_{k=1}^K$ and their corresponding log-likelihoods $\log \mathcal{L}_k$:

$$\log p(\mathbf{y} \mid M) \approx \log\left(\sum_{k=1}^{K} w_k \cdot \exp(\log \mathcal{L}_k)\right) \tag{7}$$

Given prior weights $w_k \geq 0$ with the constraint $\sum_{k=1}^{K} w_k = 1$. Uniform weights were used for both the mafic and ultramafic sample sets. Finally, we compute the posterior probability for each model using Bayes' rule:

$$p(M_i \mid \mathbf{y}) = \frac{p(\mathbf{y} \mid M_i) \cdot p(M_i)}{\sum_j p(\mathbf{y} \mid M_j) \cdot p(M_j)} \tag{8}$$

Where the denominator serves as a normalizing constant to ensure that the posterior probabilities over all models sum to 1. These posterior probabilities reflect how plausible each model is after observing the data, while accounting for the range of possible compositions and prior beliefs in each model. As an example, the posterior probability of the mafic model becomes:

$$P_{\text{mafic}} = \frac{p(\mathbf{y} \mid M_{\text{mafic}}) \cdot p(M_{\text{mafic}})}{p(\mathbf{y} \mid M_{\text{mafic}}) \cdot p(M_{\text{mafic}}) + p(\mathbf{y} \mid M_{\text{ultramafic}}) \cdot p(M_{\text{ultramafic}})} \tag{9}$$

Uncertainty assessment

To assess how uncertainty in model parameters affects the posterior probability of ultramafic and mafic rock compositions, we employed a Latin Hypercube Sampling (LHS) approach, drawing 1,000 parameter sets from uniform distributions within the following ranges: Early-areotherm = 12.0–20.0 °C/km, modern-areotherm = 7.0–11.0 °C/km, XH_2O_{mafic} = 0.0–5.0 wt%, XFe^{3+}_{mafic} = 0.0–0.5, $XH_2O_{\text{ultramafic}}$ = 0.0–5.0 wt%, and $XFe^{3+}_{\text{ultramafic}}$ = 0.0–0.3. Additionally, a subset of 20 random compositions were chosen from the mafic sample set for each iteration. This was performed to ensure particular subsets of compositions were not overly impacting the posterior. For each parameter combination, the model likelihood was computed, and marginal likelihoods for ultramafic and mafic compositions were obtained by summing across all realizations. These marginal likelihoods were then used to approximate the posterior probability of each lithology. The resulting posterior probabilities are provided in Supplementary Table S2.

Thermal modelling

The thermal modelling used a combination of internal heating from radiodecay and heat flux to the base of the crust.

$$T = -\frac{A_o z^2}{2k} + \frac{A_o H_c + q_b}{k} z + T_o \tag{10}$$

Where T is temperature, A_o is radioactive heat production (6.16×10^{-7} W/m^3)[45], H_c is crustal thickness (38 km), z is depth, q_b is basal heat flux, and k is thermal conductivity (2.5 W/m/k)[45].

Data and code availability

All input geochemical data are compiled from the published literature cited herein. The MAGEMin thermodynamic software is publicly available. Derived model outputs (velocity profiles, posterior probability tables) and code used for analysis are available at https://github.com/TMackay-Champion.

References

30. Udry, A. *et al.* What Martian Meteorites Reveal About the Interior and Surface of Mars. *Journal of Geophysical Research: Planets* **125**, e2020JE006523 (2020). URL https://agupubs.onlinelibrary.wiley.com/doi/10.1029/2020JE006523.

31. Udry, A. *et al.* A Mars 2020 *Perseverance* SuperCam Perspective on the Igneous Nature of the Máaz Formation at Jezero Crater and Link With Séítah, Mars. *Journal of Geophysical Research: Planets* **128**, e2022JE007440 (2023). URL https://agupubs.onlinelibrary.wiley.com/doi/10.1029/2022JE007440.

32. Wänke, H. & Dreibus, G. Chemistry and accretion history of Mars. *Philosophical Transactions of the Royal Society of London. Series A: Physical and Engineering Sciences* **349**, 285–293 (1994). URL https://royalsocietypublishing.org/doi/10.1098/rsta.1994.0132.

33. Morgan, J. W. & Anders, E. Chemical composition of Mars. *Geochimica et Cosmochimica Acta* **43**, 1601–1610 (1979). URL https://linkinghub.elsevier.com/retrieve/pii/0016703779901807.

34. Sanloup, C., Jambon, A. & Gillet, P. A simple chondritic model of Mars. *Physics of the Earth and Planetary Interiors* **112**, 43–54 (1999). URL https://linkinghub.elsevier.com/retrieve/pii/S0031920198001757.

35. Lodders, K. & Fegley, B. An Oxygen Isotope Model for the Composition of Mars. *Icarus* **126**, 373–394 (1997). URL https://linkinghub.elsevier.com/retrieve/pii/S0019103596956535.

36. Taylor, G. J. The bulk composition of Mars. *Geochemistry* **73**, 401–420 (2013). URL https://linkinghub.elsevier.com/retrieve/pii/S0009281913000767.

37. Yoshizaki, T. & McDonough, W. F. The composition of Mars. *Geochimica et Cosmochimica Acta* **273**, 137–162 (2020). URL https://linkinghub.elsevier.com/retrieve/pii/S0016703720300235.

38. Ohtani, E. & Kamaya, N. The geochemical model of Mars: An estimation from the high pressure experiments. *Geophysical Research Letters* **19**, 2239–2242 (1992). URL https://agupubs.onlinelibrary.wiley.com/doi/10.1029/92GL02369.

39. Riel, N., Kaus, B. J. P., Green, E. C. R. & Berlie, N. MAGEMin, an Efficient Gibbs Energy Minimizer: Application to Igneous Systems. *Geochemistry, Geophysics, Geosystems* **23**, e2022GC010427 (2022). URL https://agupubs.onlinelibrary.wiley.com/doi/10.1029/2022GC010427.

40. Green, E. C. R. *et al.* Activity–composition relations for the calculation of partial melting equilibria in metabasic rocks. *Journal of Metamorphic Geology* **34**, 845–869 (2016). URL https://onlinelibrary.wiley.com/doi/10.1111/jmg.12211.

41. Evans, K. A. & Frost, B. R. Deserpentinization in Subduction Zones as a Source of Oxidation in Arcs: a Reality Check. *Journal of Petrology* **62**, egab016 (2021). URL https://academic.oup.com/petrology/article/doi/10.1093/petrology/egab016/6132350.

42. McSween, H. Y., Labotka, T. C. & Viviano-Beck, C. E. Metamorphism in the Martian crust. *Meteoritics & Planetary Science* **50**, 590–603 (2015). URL https://onlinelibrary.wiley.com/doi/10.1111/maps.12330.

43. Frizzell, K. R., Ojha, L. & Karunatillake, S. Bounding the unknowns of martian crustal heat flow from a synthesis of regional geochemistry and InSight mission data. *Icarus* **405**, 115700 (2023). URL https://linkinghub.elsevier.com/retrieve/pii/S0019103523002774.

44. Connolly, J. & Kerrick, D. Metamorphic controls on seismic velocity of subducted oceanic crust at 100–250 km depth. *Earth and Planetary Science Letters* **204**, 61–74 (2002). URL https://linkinghub.elsevier.com/retrieve/pii/S0012821X02009573.

45. Lee, C.-T. *et al.* Crustal thickness effects on chemical differentiation and hydrology on Mars. *Earth and Planetary Science Letters* **651**, 119155 (2025). URL https://linkinghub.elsevier.com/retrieve/pii/S0012821X24005879.

Acknowledgments

T.M.-C. and M.A.L. gratefully acknowledge OUSC for enabling and supporting this research collaboration.

Author Contributions

T.M.-C. contributed to conceptualization, methodology, formal analysis, investigation, and writing – original draft. M.A.L. contributed to methodology, formal analysis, and writing – review & editing. R.P., J.W., and J.-M.K. contributed to interpretation of data and writing – review & editing.

Competing Interests

The authors declare no competing interests.

Additional Information

Supplementary Information is available for this paper.
Correspondence and requests for materials should be addressed to T.M.-C.

Supplementary Information

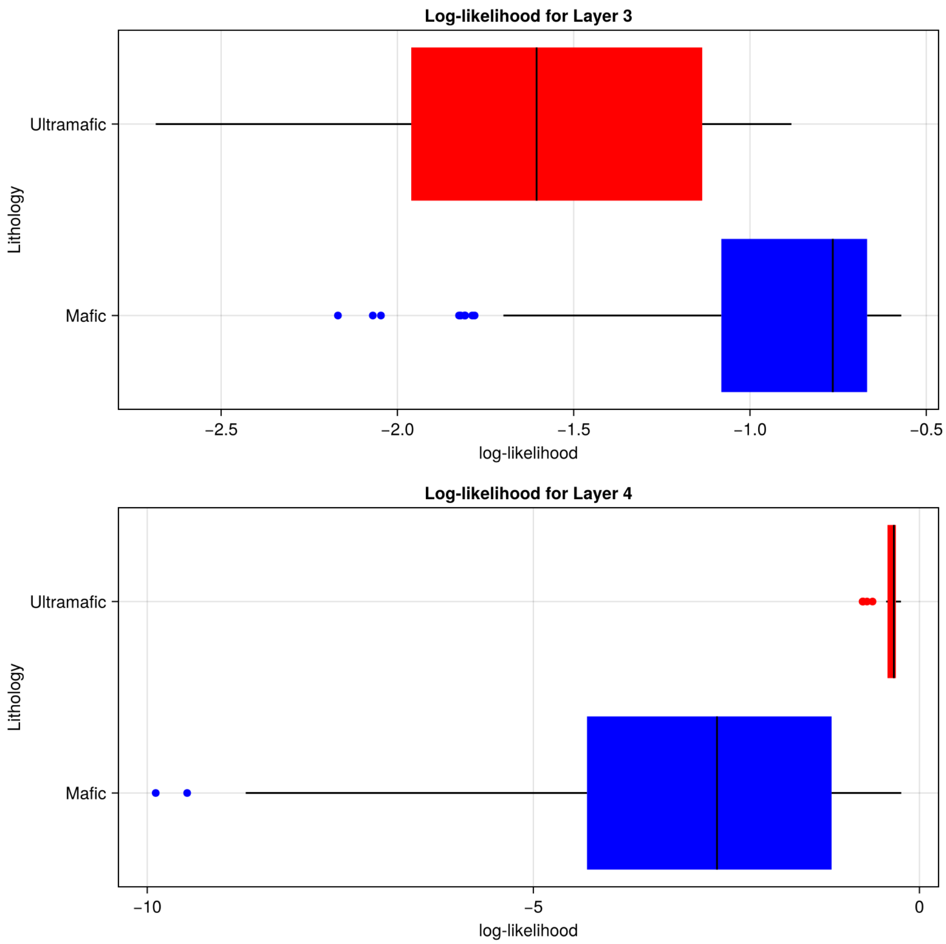

Figure S1: Log-likelihood distributions for ultramafic and mafic sample sets. Higher log-likelihood indicates better data fit for a given sample. Layer 3 log-likelihoods favour mafic compositions, whereas Layer 4 strongly favours ultramafic compositions.

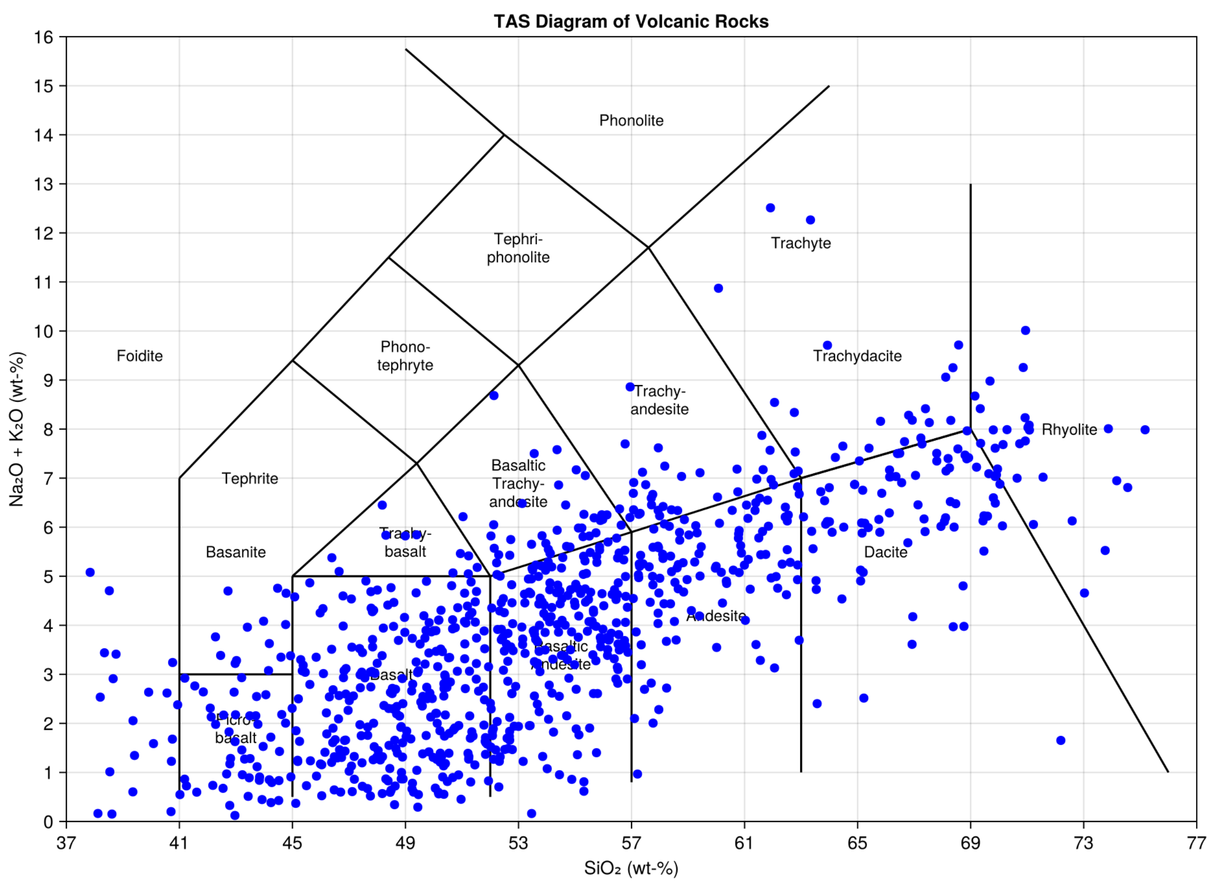

Figure S2: TAS diagram for the whole sample database.

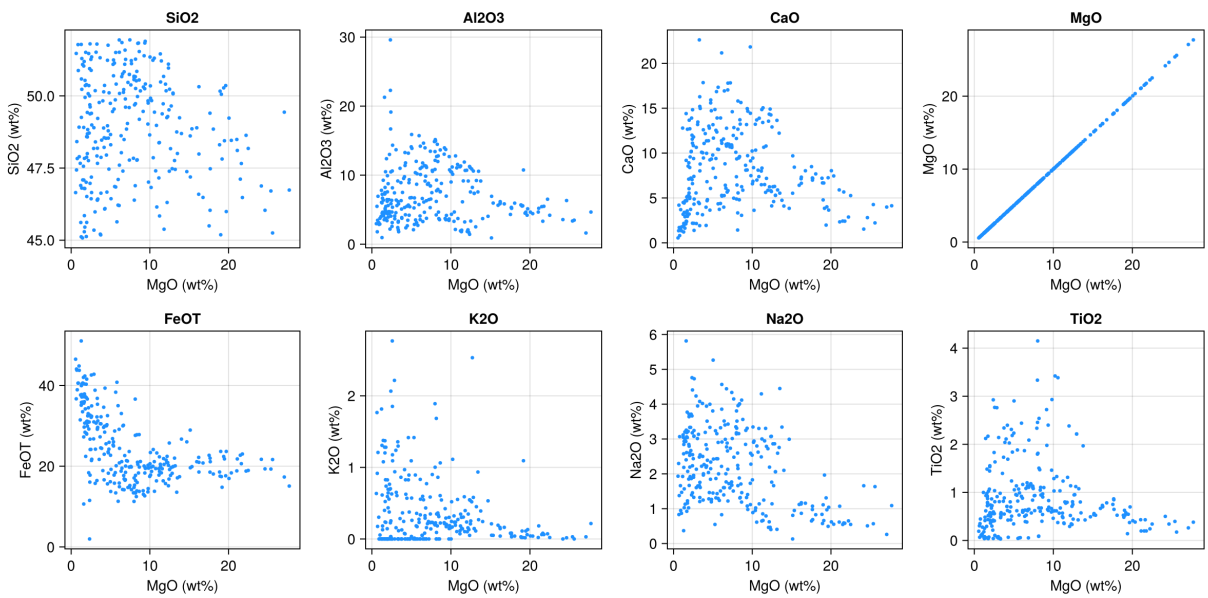

Figure S3: Geochemical variability of the basaltic compositions used in the mafic sample set. Scatter plots of major oxides versus MgO for the basaltic subset (45–52 wt% SiO_2).

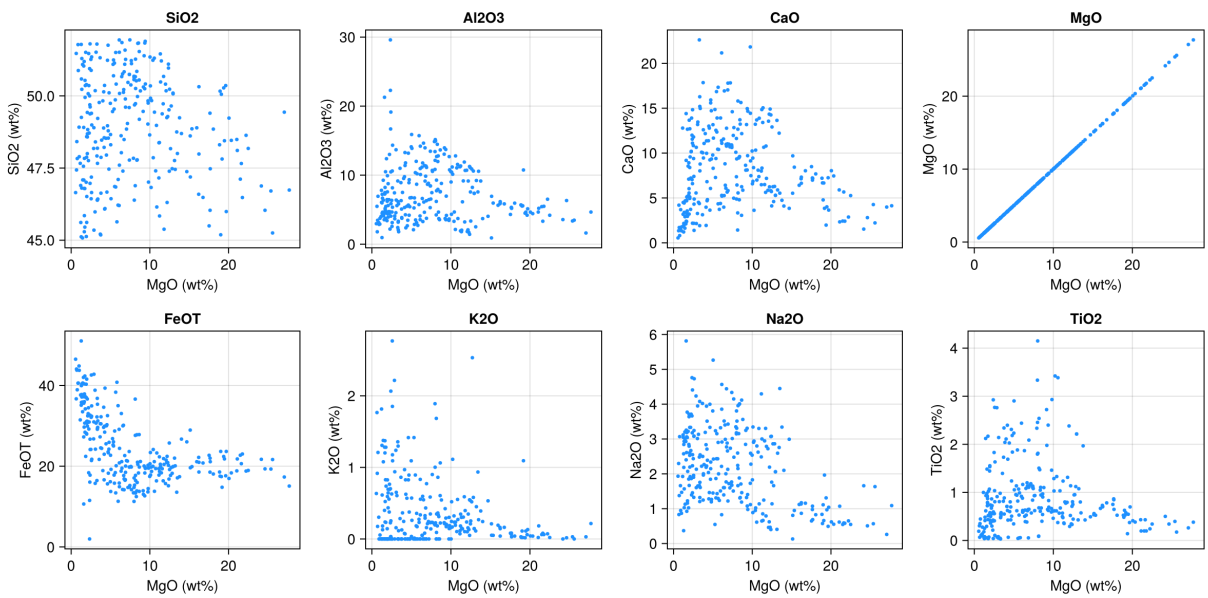

Figure S4: Geochemical variability of the ultramafic compositions (SiO_2 < 45 wt%). Scatter plots of major oxides versus MgO.

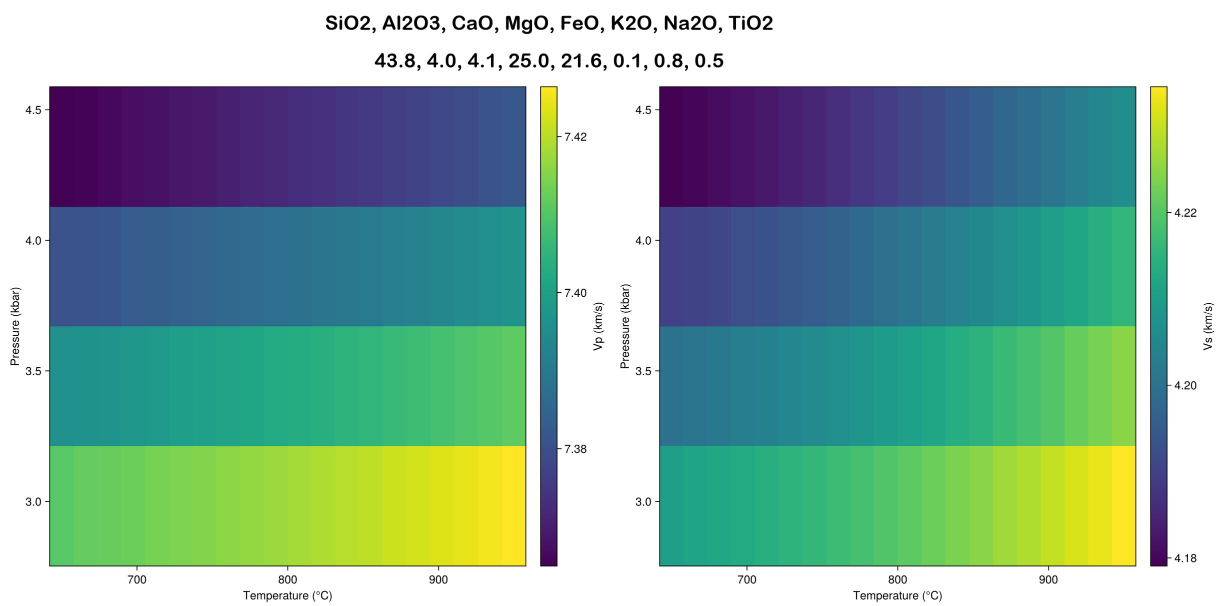

Figure S5: Seismic velocities for the medoid ultramafic composition at the elevated temperatures expected of the lower crust in a transcrustal magma system. The modern-day areotherm remains at 10 °C/km for these calculations. Unroofing was considered negligible, so the pressure was assumed to remain constant. The P-wave velocity and the S-wave velocity fit the geophysical observations of 7.8 ± 0.5 km/s and 4.1 ± 0.3 km/s, respectively. The composition of the medoid sample is given in oxide wt%.

Table S1: Posterior probability estimates evaluated with a Gaussian likelihood function, using a standard deviation equal to the reported seismic velocity uncertainty. Prior probability is the probability assigned to a parameter before considering the data; posterior probability is the probability of the parameter after incorporating the data. M = mafic, UM = ultramafic. Under uniform priors, Layer 4 is 79.2 % likely to be of ultramafic composition, while Layer 3 is 64.4 % likely to be of mafic composition.

Prior(M)	Prior(UM)	Posterior(M)	Posterior(UM)
0.5	0.5	0.644128858	0.355871142
0.6	0.4	0.730821635	0.269178365
0.7	0.3	0.808551875	0.191448125
0.8	0.2	0.878641123	0.121358877
0.9	0.1	0.942163277	0.057836723
1.0	0.0	1.000000000	0.000000000

Layer 3

Prior(M)	Prior(UM)	Posterior(M)	Posterior(UM)
0.5	0.5	0.208402461	0.791597539
0.6	0.4	0.283103915	0.716896085
0.7	0.3	0.380533567	0.619466433
0.8	0.2	0.512925214	0.487074786
0.9	0.1	0.703212472	0.296787528
1.0	0.0	1.000000000	0.000000000

Layer 4

Table S2: Posterior probability computed using Latin Hypercube Sampling to examine the impact of model parameter uncertainty. M = mafic, UM = ultramafic. Layer 4 is 71.2 % likely to be of ultramafic composition.

Prior(M)	Prior(UM)	Posterior(M)	Posterior(UM)
0.5	0.5	0.2876655476	0.7123344523
0.6	0.4	0.3772389909	0.6227610090
0.7	0.3	0.4851415848	0.5148584151
0.8	0.2	0.6176405067	0.3823594932
0.9	0.1	0.7842276704	0.2157723295
1.0	0.0	1.0000000000	0.0000000000